RESEARCH ARTICLE

NANO · MICRO small
www.small-journal.com

Protonation of Covalent Organic Framework with Robust Built-In Electric Field for Dual Electrochemiluminescence Enhancement

Xueting Cao, Wenjie Gao, Wenqi Chu, Linlin Song, Lin Cheng, Hengchang Gao, Xiaoran Zou, Kewei Ren, Huangxian Ju,* and Lin Cui**

Covalent organic frameworks (COFs) have emerged as promising electrochemiluminescence (ECL) emitters. To achieve the application, herein a dual ECL enhancement strategy is proposed for imine-linked COF by incorporating bipyridine units and implementing a post-modification method. After duplex protonation of bipyridine and imine nitrogen facilitated with ascorbic acid as a sacrificial agent, the $HCOF_{Py\text{-}Bpy}$ exhibits a robust built-in electric field, reduced bandgap, and improved hydrophilicity, resulting in 9.63- or 4.11-fold ECL enhancement with tripropylamine as coreactant compared to COFs without protonation ($COF_{Py\text{-}Bpy}$) or with protonated imine nitrogen ($HCOF_{Py\text{-}PB}$). The ECL efficiency of 20.85% is 5.27- and 2.35-fold higher than those of $COF_{Py\text{-}Bpy}$ and $HCOF_{Py\text{-}PB}$, respectively. Density functional theory calculations confirm that the protonated nitrogen in $HCOF_{Py\text{-}Bpy}$ enhances the electron-withdrawing effect and enables a large dipole moment, which alters charge distribution to strengthen the D-A effect and thus enhances ECL performance. Utilizing $HCOF_{Py\text{-}Bpy}$ as the emitter, an efficient ECL sensing platform is developed for ultrasensitive detection of iodide (I^-) and iodixanol, which demonstrates a rational post-synthetic approach to design highly efficient ECL COF emitters, offering broad sensing applications.

1. Introduction

Covalent organic frameworks (COFs) are a new kind of crystalline porous material formed through covalent bonds to reach a thermodynamic energy minimum.[1–4] The high porosity and functionality inherited from structural regularity endow them with superior potential in various fields, including gas adsorption,[5] optoelectronics,[6] sensing,[7] drug delivery,[8,9] and catalysis.[10,11] Imine-linked COFs have been widely studied due to the facile synthesis method and abundant synthetic species. In recent years, protonation-based post-synthetic modification of imine-linked COFs has been reported as a simple and effective post-treatment strategy for boosting photocatalytic activity.[12] The protonation of the functional units such as imine, amine, and triazine, even porphyrin centers, has been proposed to upgrade the activity levels for photocatalytic H_2O_2 synthesis.[13] Inspired by the protonation enhancement, this work designed a strategic implementation of post-synthetic protonation in imine-based COFs to break through the limitation of electrochemiluminescence (ECL) efficiency of COFs through simultaneously enhancing charge separation efficiency and constructing an appropriate hydrophilic interface.

ECL has garnered significant attention owing to its excellent performance.[14–17] The predesignable topologies and functionalities of COFs enable their action as ECL emitters for investigating fundamental ECL mechanisms. COFs can not only immobilize ECL-active molecules with great capacity but also function as intrinsic ECL-active species to yield superior ECL intensity. As reticular emitters, the ECL efficiency of COFs is determined by intrareticular charge transfer-mediated radical annihilation.[18–20] Nevertheless, the issue of sluggish charge transfer between ECL emitters and co-reactants/emitters in most COFs is still difficult to solve, which leads to unsatisfactory ECL performance. In pursuit of improving the ECL efficiency of COFs, a series of strategies have been conducted, such as donor-acceptor (D-A) design strategy,[18,20] integration of luminophore and co-reactant units to shorten the distance between anion/cation radicals,[19,21] and introduction of conjugated linkages for extended π-conjugation.[22] However, their improvements are limited. As a post-synthetic modification approach that offers unique advantages in introducing functionalities, the protonation treatment represents the

X. Cao, W. Gao, W. Chu, L. Song, L. Cheng, H. Gao, X. Zou, L. Cui
College of Chemistry, Chemical Engineering and Materials Science
Shandong Normal University
Jinan 250014, China
E-mail: cuilin@sdnu.edu.cn

K. Ren
School of Chemistry and Chemical Engineering
Nanjing University of Science and Technology
Nanjing 210094, China
E-mail: kwren@njust.edu.cn

H. Ju
State Key Laboratory of Analytical Chemistry for Life Science, School of Chemistry and Chemical Engineering
Nanjing University
Nanjing 210023, China
E-mail: hxju@nju.edu.cn

The ORCID identification number(s) for the author(s) of this article can be found under https://doi.org/10.1002/smll.202510880

DOI: 10.1002/smll.202510880

most straightforward approach for post-synthetic modification of COFs, though this strategy remains unexplored in the ECL field.

Herein, we used pyrene with benzidine and bipyridine to synthesize two imine-linked COFs ($COF_{Py\text{-}PB}$ and $COF_{Py\text{-}Bpy}$) via Schiff-base condensation, respectively, and designed a facile post-protonation strategy to enhance their ECL performance. After simultaneous post-protonation of bipyridine nitrogen and imine nitrogen, the ECL efficiency of dual protonated COF ($HCOF_{Py\text{-}Bpy}$) showed notable improvement with tripropylamine (TPrA) as a co-reactant in a low potential range from 0 to +0.8 V. Compared with COFs without protonation and the only protonated imine nitrogen ($HCOF_{Py\text{-}PB}$), $HCOF_{Py\text{-}Bpy}$ exhibited 9.63- and 4.11-fold enhancement in ECL intensity, respectively. Due to protonated nitrogen atoms exerting a stronger electron-withdrawing effect, $HCOF_{Py\text{-}Bpy}$ enabled a larger dipole moment, exhibited a robust built-in electric field, and improved hydrophilicity, which altered the charge distribution, thus regulating the D-A effect in $HCOF_{Py\text{-}Bpy}$ to enhance the ECL performance. The $HCOF_{Py\text{-}Bpy}$ could be used for the highly efficient detection of iodide ions (I^-). This work enhances the ECL performance of COF-based emitters, highlighting the advantage of dual protonation in the design of effective ECL emitters.

2. Results and Discussion

2.1. Characterizations of COFs

Two imine-linked pyrene-based COFs were constructed through a Schiff-base condensation reaction of 1,3,6,8-tetra(4-formylphenyl)pyrene (Py) with benzidine (PB) or 2,2′-bipyridine-5,5′-diamine (Bpy) to obtain the corresponding $COF_{Py\text{-}PB}$ and $COF_{Py\text{-}Bpy}$. Subsequently, the protonated $COF_{Py\text{-}PB}$ and $COF_{Py\text{-}Bpy}$ (denoted as $HCOF_{Py\text{-}PB}$ and $HCOF_{Py\text{-}Bpy}$) were prepared using ascorbic acid as a sacrificial agent. Compared with $HCOF_{Py\text{-}PB,}$ which only protonated the imine nitrogen, $HCOF_{Py\text{-}Bpy}$ simultaneously protonated both the imine nitrogen and pyridine nitrogen (**Figure 1A**). The crystalline structures of COFs were elucidated by experimental and simulated powder X-ray diffraction (PXRD) patterns. $COF_{Py\text{-}PB}$ displayed a primary reflection at 3.04° assigned to the (100) plane, accompanied by weaker peaks at 4.20° (110), 6.26° (200), and 9.48° (300) (Figure 1B). Similarly, $COF_{Py\text{-}Bpy}$ showed diffraction peaks at 3.36°, 4.54°, 6.56°, and 9.68° corresponding to the (110), (020), (220), and (330) facets, respectively (Figure 1D). The PXRD of $HCOF_{Py\text{-}PB}$ and $HCOF_{Py\text{-}Bpy}$ are almost identical to the pristine $COF_{Py\text{-}PB}$ and $COF_{Py\text{-}Bpy}$, indicating that the protonated COFs possessed iso-reticular framework structures.[23] Upon protonation, the crystallinity of $HCOF_{Py\text{-}PB}$ was well maintained, as evidenced by the intense peak at 3.02°, along with multiple peaks at 4.26°, 6.22°, and 9.42° originating from the (100), (110), (200), and (300) facets, respectively (Figure 1C). $HCOF_{Py\text{-}Bpy}$ was highly crystalline with diffraction peaks at 3.32°, 4.52°, 6.58°, and 9.62°, which were assignable to (110), (020), (220), and (330) facets, respectively (Figure 1E). Four COFs with AA and AB stacking were modelled structurally (Figures 1F–I; Figure S1, Supporting Information). The experimentally observed PXRD profiles aligned more closely with the simulated AA-stacked eclipsed configuration than those with the staggered AB stacking pattern. Further Pawley refinements gave the unit cell parameters of a = 28.25 Å, b = 28.65 Å, c = 3.76 Å, $\alpha = \beta = \gamma = 90°$, R_p = 7.52% and R_{wp} = 9.87% for $COF_{Py\text{-}PB}$; a = 28.58 Å, b = 28.96 Å, c = 3.75 Å, $\alpha = \beta = \gamma = 90°$, R_p = 5.90% and R_{wp} = 7.68% for $HCOF_{Py\text{-}PB}$; a = 28.16 Å, b = 28.60 Å, c = 3.76 Å, R_p = 6.22% and R_{wp} = 7.80% for $COF_{Py\text{-}Bpy}$; and a = 28.29 Å, b = 28.63 Å, c = 3.78 Å, R_p = 5.33% and R_{wp} = 6.89% for $HCOF_{Py\text{-}Bpy}$. The high crystalline structure with the AA stacking arrangement facilitated efficient charge carrier mobility.[24,25] These results collectively indicated that the protonation modification led to a negligible effect on the crystal structure.

All COFs exhibited type-IV sorption isotherms (**Figure 2A–D**). Among them, $COF_{Py\text{-}PB}$ and $HCOF_{Py\text{-}PB}$ have mesoporous structures, while $COF_{Py\text{-}Bpy}$ and $HCOF_{Py\text{-}Bpy}$ have microporous-mesoporous structures.[26] The Brunauer-Emmett-Teller (BET) surface areas of $COF_{Py\text{-}PB}$, $HCOF_{Py\text{-}PB}$, $COF_{Py\text{-}Bpy}$, and $HCOF_{Py\text{-}Bpy}$ were 1168, 904, 1531, and 1360 $m^2\ g^{-1}$, respectively (Figure 2A–D). The BET surface areas of $HCOF_{Py\text{-}PB}$ and $HCOF_{Py\text{-}Bpy}$ were slightly decreased after protonation treatment. The pore size distributions of $COF_{Py\text{-}PB}$, $HCOF_{Py\text{-}PB}$, $COF_{Py\text{-}Bpy}$, and $HCOF_{Py\text{-}Bpy}$ were centered at 2.16, 2.16, 1.27 / 2.16, and 1.27 / 2.16 nm, as estimated by nonlocal density functional theory (insets in Figure 2A–D). The scanning electron microscopic (SEM) images showed the rodlike structure of $COF_{Py\text{-}PB}$ (Figure S2A, Supporting Information) and the nanoflower shape of $COF_{Py\text{-}Bpy}$ (Figure S2C, Supporting Information). The morphological characteristics exhibited negligible variation after protonation, demonstrating that the post-synthesis modification did not change the morphological structure (Figure S2B–D, Supporting Information).[27] Furthermore, high-resolution transmission electron microscopic (HR-TEM) images of COFs exhibited clear lattice fringes throughout the sample, indicating their high crystallinity. Both $COF_{Py\text{-}PB}$ and $HCOF_{Py\text{-}Bpy}$ exhibited 2.31 nm lattice fringes in HR-TEM images, consistent with the (100) plane (Figure 2E,F). Furthermore, HR-TEM analysis of $COF_{Py\text{-}Bpy}$ and $HCOF_{Py\text{-}Bpy}$ reveals distinct lattice fringe spacings of 2.18 nm, which align with the (110) plane (Figure 2G,H). In addition, the composition and surface structure of COFs were elucidated by X-ray photoelectron spectroscopy (XPS). All four COFs showed three peaks belonging to C, N, and O elements (Figure S3, Supporting Information). In N 1s spectra, all the COFs showed the split peaks of the imine group (Figure 2I–L), implying the successful synthesis of imine COFs. Additionally, splitting of the pyridine N bond occurred at 398.47 and 398.31 eV for $COF_{Py\text{-}Bpy}$ and $HCOF_{Py\text{-}Bpy}$ (Figure 2K,L), which was indicative of the introduction of the pyridine N.[27] $HCOF_{Py\text{-}PB}$ showed a new split peak at 400.10 eV ascribed to N—H compared to $COF_{Py\text{-}PB}$ (Figure 2J), further proving successful protonation of imine N.[13] In addition, upon protonation, imine N and pyridine N peaks of $HCOF_{Py\text{-}Bpy}$ were shifted, indicating that imine N and pyridine N were protonated to N—H, with a peak at 400.63 eV (Figure 2L).[13,23,27]

The Fourier transform infrared (FTIR) spectra of $COF_{Py\text{-}PB}$ and $COF_{Py\text{-}Bpy}$ showed C═N bond stretching signals at 1622 and 1624 cm^{-1}, whereas the aldehyde band almost disappeared at 1695 cm^{-1}, confirming the formation of imine bonds in two COFs (**Figure 3A,B**). Compared with the FTIR spectra of original $COF_{Py\text{-}PB}$ and $COF_{Py\text{-}Bpy}$, $HCOF_{Py\text{-}PB}$ and $HCOF_{Py\text{-}Bpy}$

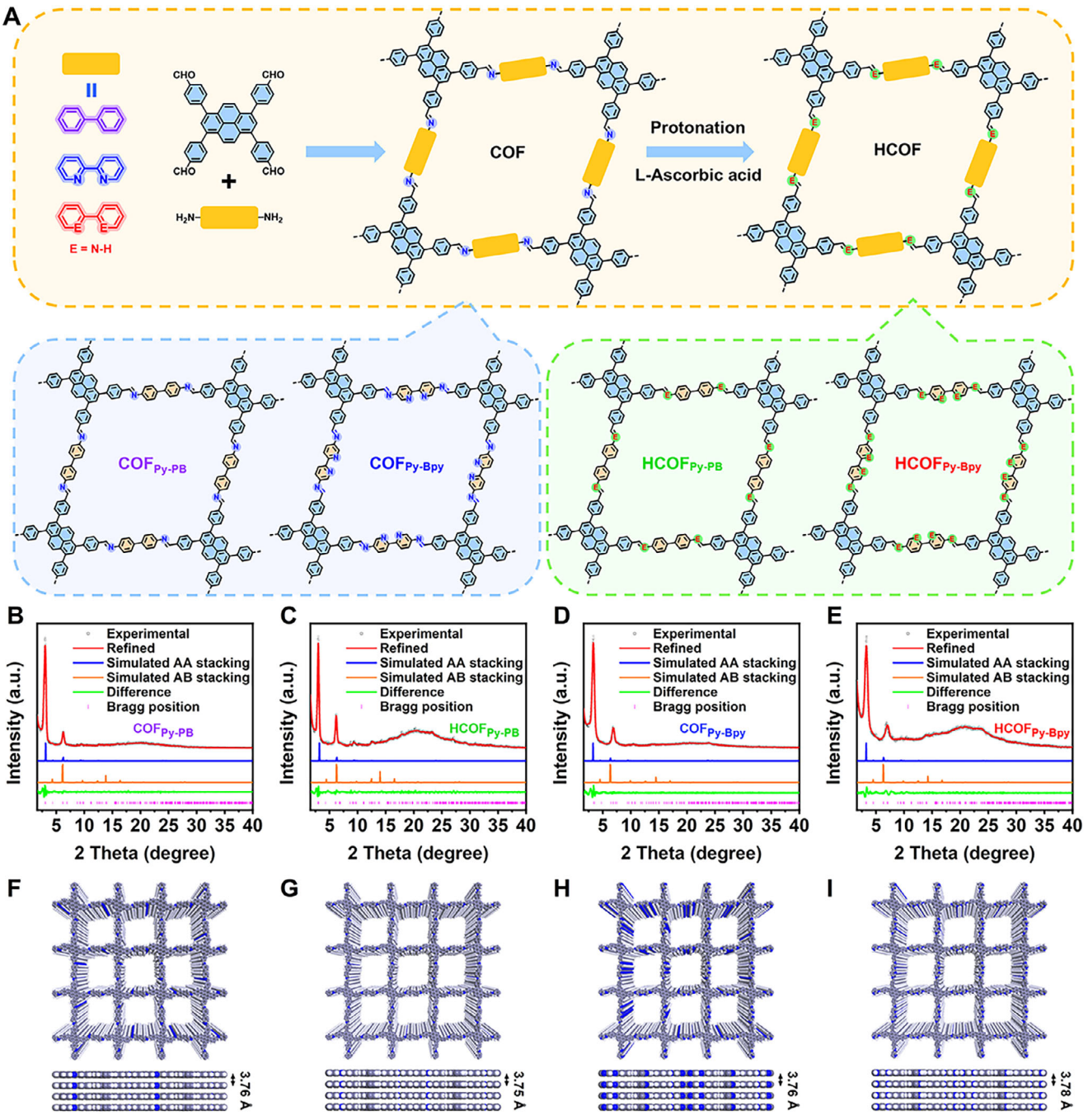

Figure 1. A) Schematic of preparation and structure of $COF_{Py\text{-}PB}$, $HCOF_{Py\text{-}PB}$, $COF_{Py\text{-}Bpy}$, and $HCOF_{Py\text{-}Bpy}$. B–E) PXRD patterns of $COF_{Py\text{-}PB}$ (B), $HCOF_{Py\text{-}PB}$ (C), $COF_{Py\text{-}Bpy}$ (D), and $HCOF_{Py\text{-}Bpy}$ (E). Pawley refinement (red curve), experimental profile (black dots), simulated patterns of AA (blue curve) and AB (orange curve) stacking models, difference (green curve), and Bragg position (pink short sticks). F–I) Top and side views of the eclipsed AA stacking models of $COF_{Py\text{-}PB}$ (F), $HCOF_{Py\text{-}PB}$ (G), $COF_{Py\text{-}Bpy}$ (H), and $HCOF_{Py\text{-}Bpy}$ (I).

exhibited new peaks at 1653 and 1670 cm^{-1}, which were attributed to the transfer of the characteristic peak of the protonated imine C═N bond (Figure 3A, green curve and 3B, red curve), known as the C═NH^+ bond stretching vibration.[28] Meanwhile, a new peak at 3200-3500 cm^{-1} appeared in the FTIR spectrum of $HCOF_{Py\text{-}Bpy}$ compared to pristine $COF_{Py\text{-}Bpy}$ (Figure 3B, red curve), assigned to the N—H stretching vibration of the protonated pyridine groups.[23] UV–vis diffuse reflectance spectroscopic (UV–vis DRS) analyses were conducted to explore the light-related characteristics. These COFs exhibited a notable bathochromic shift in their absorption edge relative to their precursor ligands, which could be attributed to the enhanced π-conjugation network formed during framework assembly (Figure S4, Supporting Information).[29] The optical bandgaps

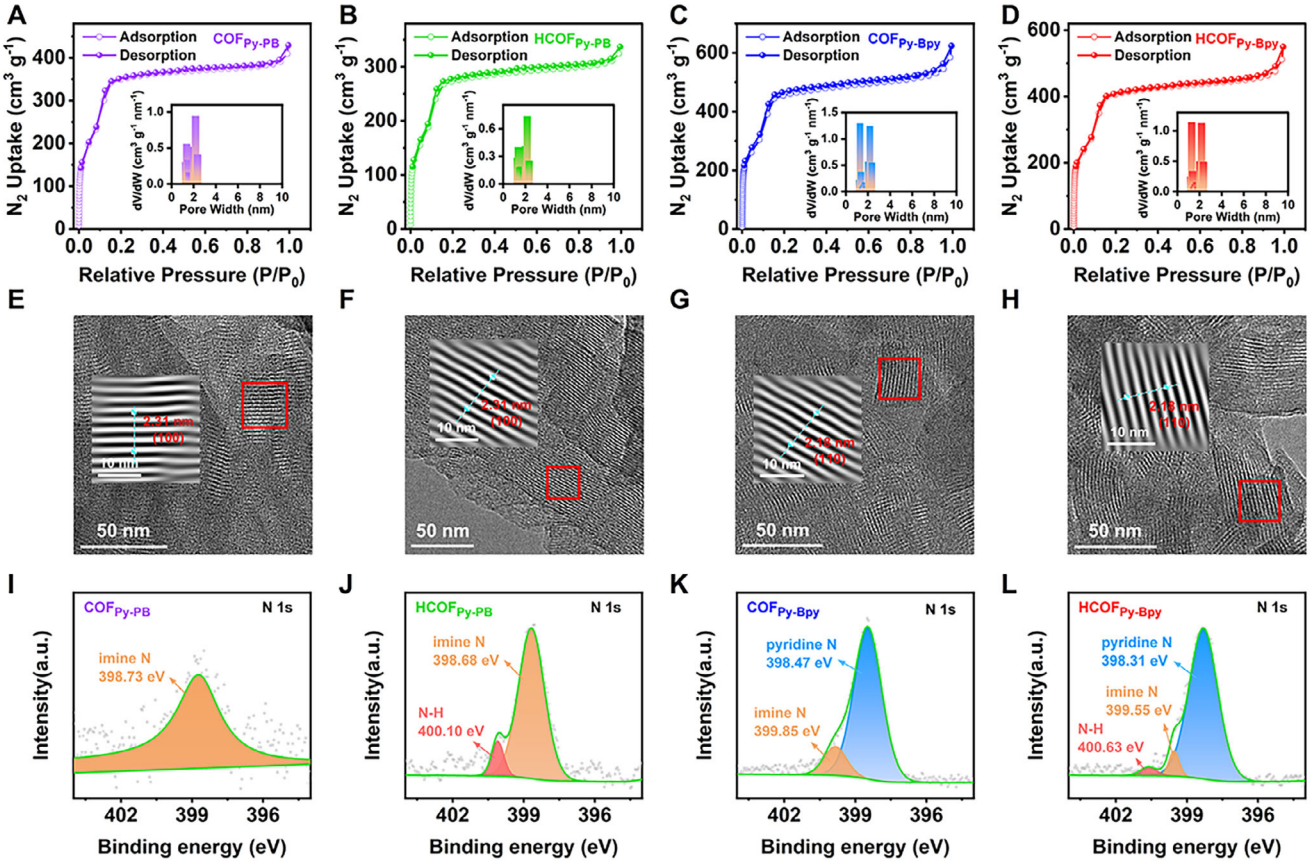

Figure 2. A–D) N_2 sorption curves and corresponding pore size distributions, E–H) HR-TEM images, and I–L) N 1s XPS spectra of COF_{Py-PB} (A,E,I), $HCOF_{Py-PB}$ (B,F,J), COF_{Py-Bpy} (C,G,K), and $HCOF_{Py-Bpy}$ (D,H,L).

of COF_{Py-PB} and COF_{Py-Bpy}, $HCOF_{Py-PB}$ and $HCOF_{Py-Bpy}$ calculated from Tauc plots were ≈2.32, 2.10, 2.28, and 2.04 eV, respectively (Figure 3C,D).

After protonation, the reduced bandgap was beneficial to the carrier migration of the conjugate skeleton. As shown in the photoluminescence (PL) spectra (Figure 3E), $HCOF_{Py-Bpy}$ (555 nm) exhibited a redshifted maximum emission peak compared with COF_{Py-PB} (526 nm), $HCOF_{Py-PB}$ (513 nm), COF_{Py-Bpy} (538 nm), indicating its extended π-electron conjugation and enhanced D-A characteristic. The longer average PL lifetime of $HCOF_{Py-Bpy}$ (3.28 ns) compared to COF_{Py-PB} (1.81 ns), $HCOF_{Py-PB}$ (2.17 ns), COF_{Py-Bpy} (2.87 ns) (Figure 3F) indicated that protonation improved charge separation efficiency.[30–32] The protonated $HCOF_{Py-Bpy}$ exhibited a stronger photocurrent response than COF_{Py-PB}, $HCOF_{Py-PB}$, and COF_{Py-Bpy} (Figure 3G), indicating the enhanced charge separation after the protonation. The electrochemical impedance spectroscopy (EIS) was employed to characterize the COF_{Py-PB}/GCE, $HCOF_{Py-PB}$/GCE, COF_{Py-Bpy}/GCE, $HCOF_{Py-Bpy}$/GCE, and bare GCE using a Randles equivalent circuit (i.e., Warburg impedance (Z_w), charge transfer impedance (R_{et}), solution impedance (R_s), and electrical double-layer capacitor (C_{dl}), as shown inset of Figure 3H). The protonated $HCOF_{Py-Bpy}$ (425Ω) exhibited a smaller charge transfer resistance than COF_{Py-PB} (1085Ω), $HCOF_{Py-PB}$ (571Ω), and COF_{Py-Bpy} (738Ω) (Figure 3H), indicating that the protonation possessed a higher charge transfer rate.[33] Moreover, the EIS curves of COFs showed smaller semicircles compared with the corresponding ligands, indicating that the formation of framework structures of COFs increased the charge transfer rate (Figure S5, Supporting Information). The water contact angle measurements demonstrated that the surface wettability of COFs could be systematically modulated through modifying functional groups. The water contact angles of the protonated COFs were slightly reduced (Figure 3I–L), indicating an increase in the solid-liquid contact area to promote the transfer and separation of charges. In addition, the COF_{Py-PB} and $HCOF_{Py-PB}$ decomposed at 340 °C. In contrast, COF_{Py-Bpy} and $HCOF_{Py-Bpy}$ featured more thermal stability with less than 5% mass loss to 515 °C under a N_2 atmosphere (Figure S6, Supporting Information).

2.2. ECL and Electrochemical Properties of COFs

The protonated $HCOF_{Py-Bpy}$ showed an oxidation peak at +0.98 V in PBS, which was lower than those of COF_{Py-PB}, $HCOF_{Py-PB}$, and COF_{Py-Bpy} (**Figure 4A**). The co-reactant TPrA showed an oxidation peak at +0.91 V and a weak ECL intensity of 100 a.u. on bare GCE (Figure 4B–C, orange curves). Compared to initial COFs, the protonated COFs showed stronger oxidation peak currents, indicating that they were more easily oxidized (Figure 4B).

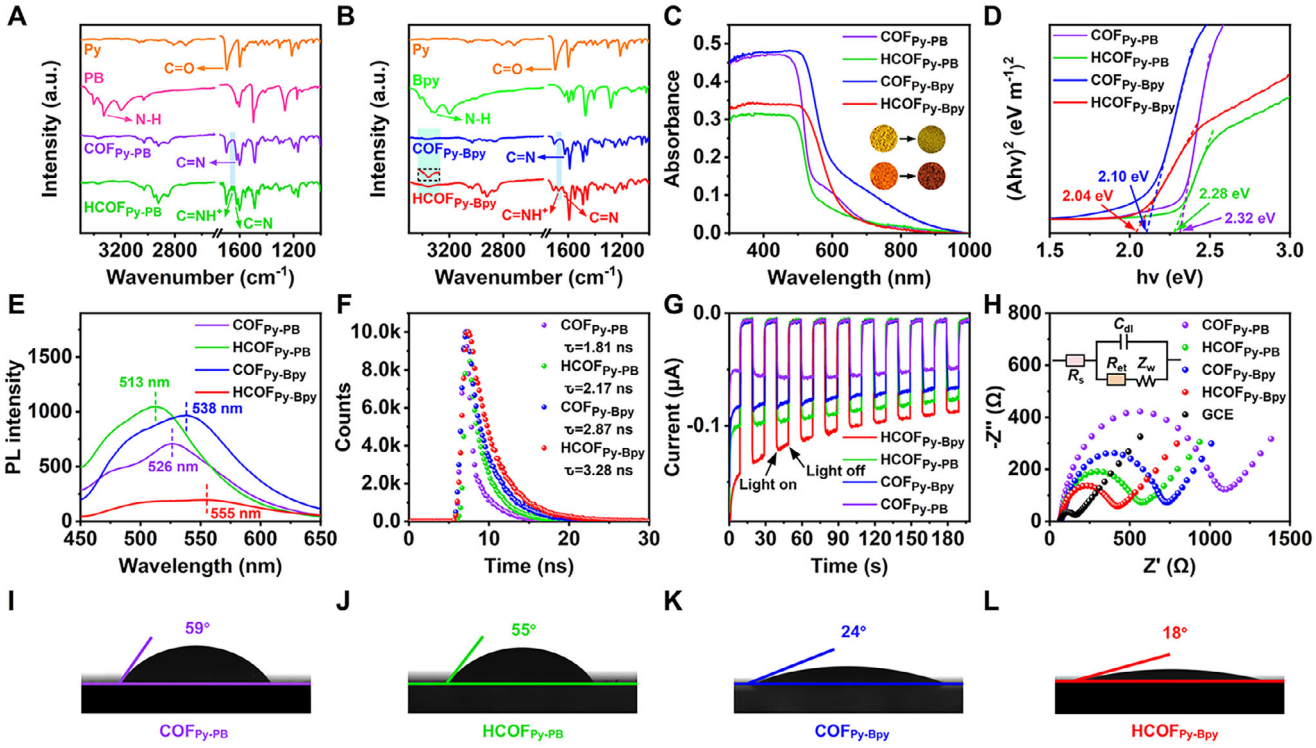

Figure 3. A) FTIR spectra of Py, PB, $COF_{Py\text{-}PB}$, and $HCOF_{Py\text{-}PB}$. B) FTIR spectra of Py, Bpy, $COF_{Py\text{-}Bpy}$, and $HCOF_{Py\text{-}Bpy}$. C) Solid-state UV–vis DRS spectra, D) Tauc plots, E) PL spectra, F) PL lifetime curves, and G) photocurrents of $COF_{Py\text{-}PB}$, $HCOF_{Py\text{-}PB}$, $COF_{Py\text{-}Bpy}$, and $HCOF_{Py\text{-}Bpy}$. H) EIS curves of GCE, $COF_{Py\text{-}PB}$/GCE, $HCOF_{Py\text{-}PB}$/GCE, $COF_{Py\text{-}Bpy}$/GCE, and $HCOF_{Py\text{-}Bpy}$/GCE in 0.1 M KCl containing 5 mM $[Fe(CN)_6]^{3-/4-}$. I–L) Contact angle goniometric images of water droplets on $COF_{Py\text{-}PB}$ (I), $HCOF_{Py\text{-}PB}$ (J), $COF_{Py\text{-}Bpy}$ (K), and $HCOF_{Py\text{-}Bpy}$ (L).

Therefore, the ECL intensities of $HCOF_{Py\text{-}PB}$ and $HCOF_{Py\text{-}Bpy}$ modified GCEs were 26.04 and 10.97-fold higher than those of $COF_{Py\text{-}PB}$ and $COF_{Py\text{-}Bpy}$, respectively. In addition, the ECL intensity of the $HCOF_{Py\text{-}Bpy}$ modified GCE with more protonation sites was 5.24-fold higher than that of the $HCOF_{Py\text{-}PB}$ modified GCE (Figure 4C). The enhanced ECL performance of the $HCOF_{Py\text{-}Bpy}$/TPrA system could be attributed to the following mechanistic pathways (Equations 1–5).

$$HCOFPy - Bpy - e- \rightarrow HCOFPy - Bpy\bullet + \quad (1)$$

$$TPrA - e- \rightarrow TPrAH\bullet + \quad (2)$$

$$TPrAH^{\bullet +} - H^{+} \rightarrow TPrA^{\bullet} \quad (3)$$

$$HCOFPy - Bpy\bullet + + TPrA\bullet \rightarrow HCOFPy - Bpy* + Pr2N + HC = CH2CH3 \quad (4)$$

$$HCOFPy - Bpy* \rightarrow HCOFPy - Bpy + hv \quad (5)$$

In order to maximize the ECL performance of $HCOF_{Py\text{-}Bpy}$, the experimental conditions were optimized, including the types of co-reactants, potential window, and scan rate (Figure 4D–F). $HCOF_{Py\text{-}Bpy}$ produced the strongest ECL intensity in TPrA system (Figure 4D). The $HCOF_{Py\text{-}Bpy}$/TPrA generated the highest ECL intensity in the potential range from 0 to +0.8 V (Figure 4E), which was due to the fact that both $HCOF_{Py\text{-}Bpy}$ and TPrA were oxidized to their respective radicals at a starting potential of +0.60 V (Figure 4B, red and orange curves). The concentration and stability of $HCOF_{Py\text{-}Bpy}^{\bullet +}$ and $TPrAH^{\bullet +}$ reached an optimal equilibrium in this potential window.[34] The scan rate of 0.3 V s^{-1} was the optimal rate for amplifying the ECL signals (Figure 4F). Under optimal conditions, the ECL intensities of $HCOF_{Py\text{-}PB}$ and $HCOF_{Py\text{-}Bpy}$ were 7.88 and 9.63-fold higher than those of $COF_{Py\text{-}PB}$ and $COF_{Py\text{-}Bpy}$, suggesting that protonation could enhance the intensity of the ECL signal. Moreover, the ECL intensity of the $HCOF_{Py\text{-}Bpy}$ with more protonation sites was 4.11-fold higher than that of the $HCOF_{Py\text{-}PB}$ (Figure 4G). The ECL signals of PB, Py, and Bpy monomers were all smaller compared to COFs in PBS or TPrA (Figure S7, Supporting Information). The relative ECL efficiencies of $HCOF_{Py\text{-}PB}$ and $HCOF_{Py\text{-}Bpy}$ were determined to be 8.89% and 20.9%, which were 4.40 and 5.27-fold higher than $COF_{Py\text{-}PB}$ (2.02%) and $COF_{Py\text{-}Bpy}$ (3.96%). The relative ECL efficiency of $HCOF_{Py\text{-}Bpy}$ was 2.35-fold higher than $HCOF_{Py\text{-}PB}$ (Figure 4H). The electroactive surface area of $HCOF_{Py\text{-}Bpy}$ (15.36 mm^2) was larger than $COF_{Py\text{-}PB}$ (9.41 mm^2), $HCOF_{Py\text{-}PB}$ (13.20 mm^2), and $COF_{Py\text{-}Bpy}$ (11.64 mm^2) (Figure 4I; Figure S8, Supporting Information), indicating a conductive interface with faster charge transport capacity to enhance the ECL signal.[35,36] The linear correlation between the peak current density of $COF_{Py\text{-}PB}$, $HCOF_{Py\text{-}PB}$, $COF_{Py\text{-}Bpy}$, and $HCOF_{Py\text{-}Bpy}$ and scan rate (Figure 4J; Figure S9, Supporting Information) confirmed an interfacial charge transfer. The smaller slopes of logarithmic plots for the protonated COFs demonstrated higher

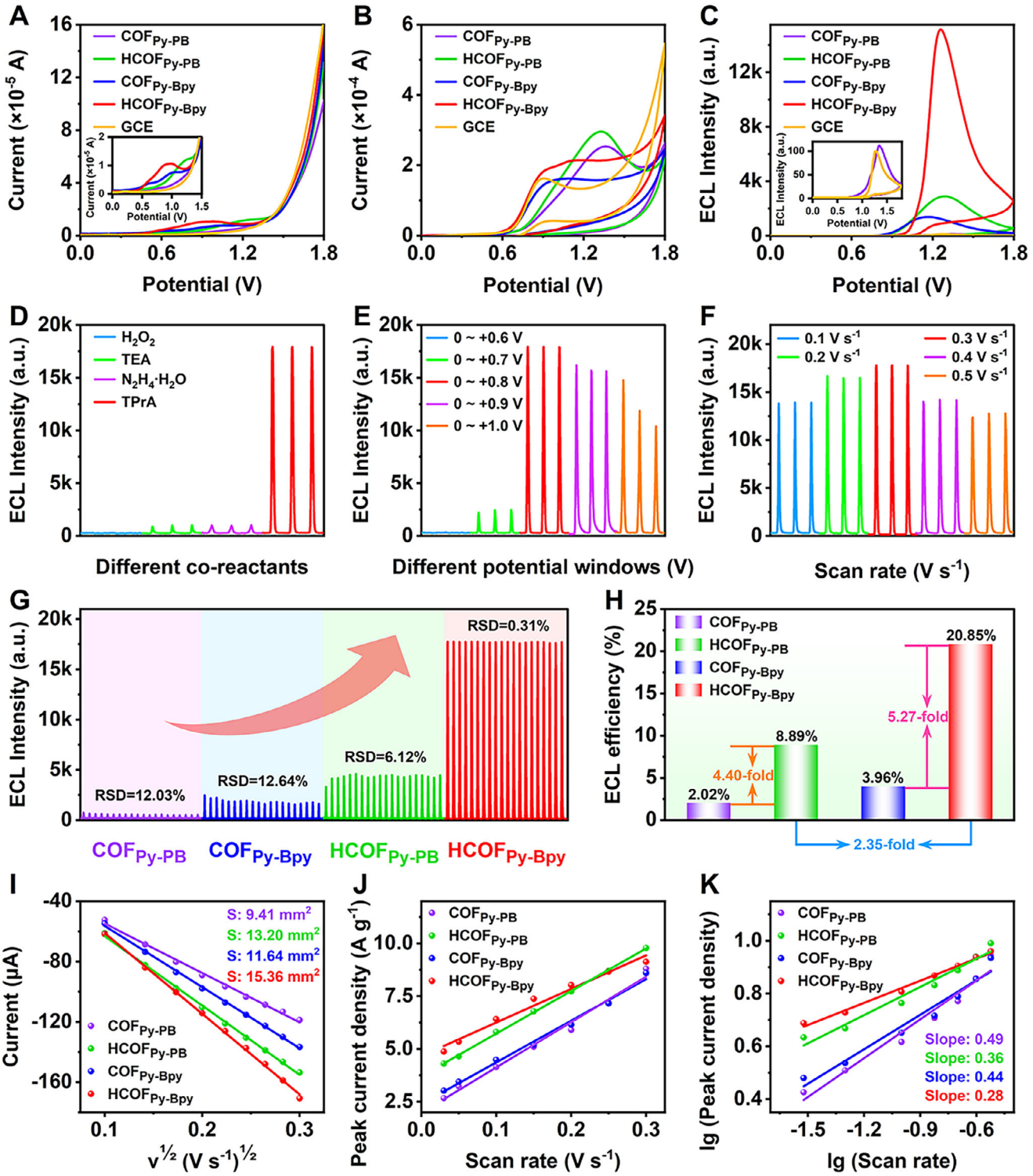

Figure 4. A) DPV curves of $COF_{Py\text{-}PB}$, $HCOF_{Py\text{-}PB}$, $COF_{Py\text{-}Bpy}$, $HCOF_{Py\text{-}Bpy}$, and GCE in 0.1 M PBS (pH 7.4). B,C) CV (B) and ECL (C) curves of $COF_{Py\text{-}PB}$, $HCOF_{Py\text{-}PB}$, $COF_{Py\text{-}Bpy}$, $HCOF_{Py\text{-}Bpy}$, and GCE in 20 mM TPrA at 0.3 V s^{-1}. PMT = 450 V. D) ECL curves of $HCOF_{Py\text{-}Bpy}$/GCE in the presence of 20 mM H_2O_2, TEA, $N_2H_4{\bullet}H_2O$ or TPrA as co-reactants. E,F) ECL curves of $HCOF_{Py\text{-}Bpy}$/GCE in 20 mM TPrA at different potential windows (E) and scan rates (F). G) Stability of ECL intensity of $COF_{Py\text{-}PB}$, $HCOF_{Py\text{-}PB}$, $COF_{Py\text{-}Bpy}$, and $HCOF_{Py\text{-}Bpy}$ modified GCEs in 20 mM TPrA at 0.3 V s^{-1}. PMT = 850 V. H) Relative ECL efficiency. I) Linear relationship between cathode peak current and the square root of scan rate. J) Plots of peak current density versus scan rate. K) Logarithmic plots of peak current density versus scan rate.

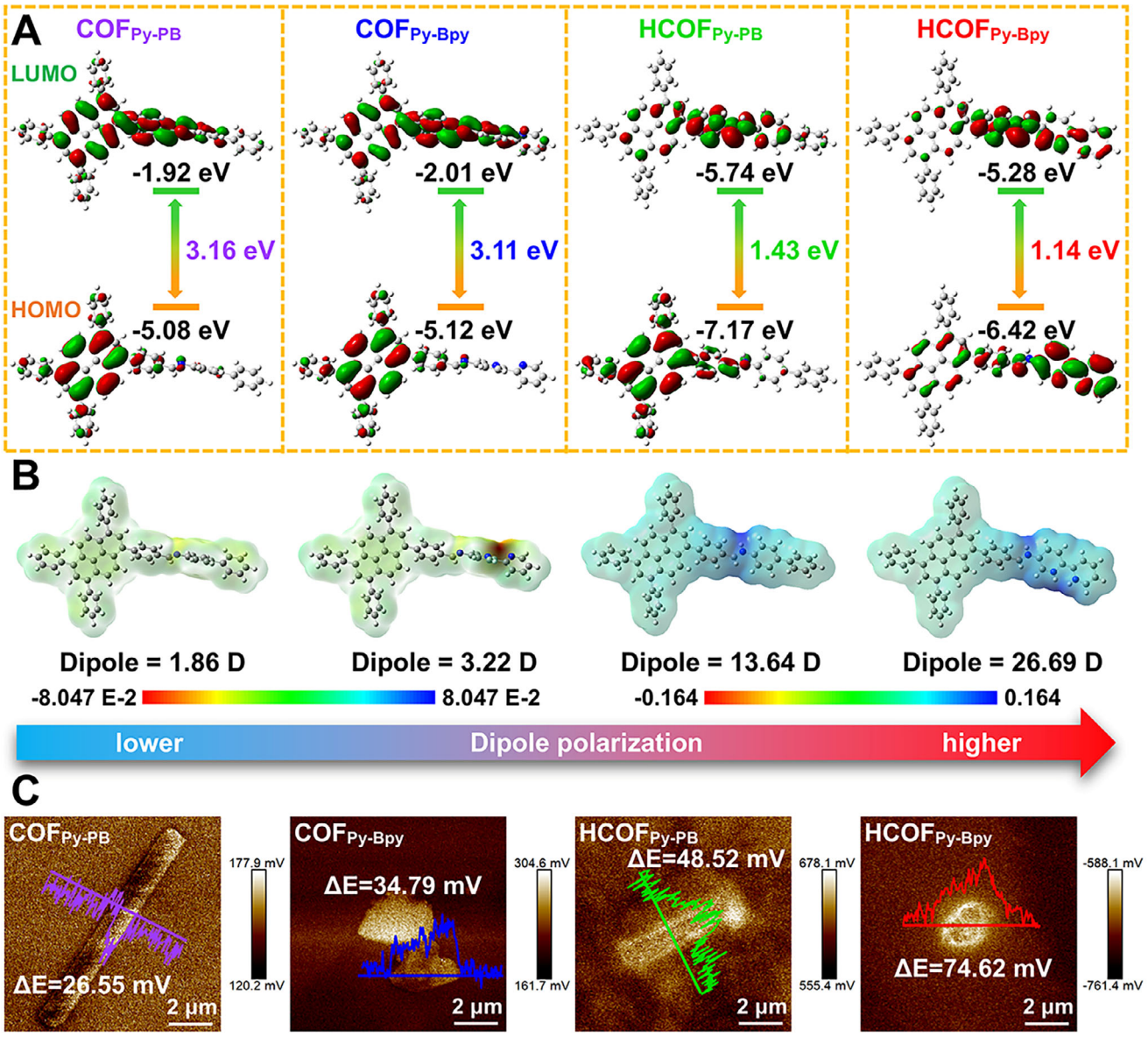

Figure 5. A) LUMO and HOMO orbitals distribution in $COF_{Py\text{-}PB}$, $COF_{Py\text{-}Bpy}$, $HCOF_{Py\text{-}PB}$, and $HCOF_{Py\text{-}Bpy}$. B) Dipole polarization ability of $COF_{Py\text{-}PB}$, $COF_{Py\text{-}Bpy}$, $HCOF_{Py\text{-}PB}$, and $HCOF_{Py\text{-}Bpy}$. C) Surface potentials of $COF_{Py\text{-}PB}$, $COF_{Py\text{-}Bpy}$, $HCOF_{Py\text{-}PB}$, and $HCOF_{Py\text{-}Bpy}$ detected with KPFM.

pseudo-activity than the original COFs (Figure 4K). Therefore, the protonation enhanced the ECL and electrochemical performance of COFs.

2.3. DFT Calculations

The electronic structure and charge transfer behavior of the smallest repeating units of four COFs were investigated by using density functional theory (DFT)[37] to calculate their highest occupied molecular orbital (HOMO) and lowest unoccupied molecular orbital (LUMO). The HOMOs of both $COF_{Py\text{-}PB}$ and $COF_{Py\text{-}Bpy}$ localized to the pyrenyl areas (**Figure** 5A). In comparison with $COF_{Py\text{-}PB}$, the LUMO of $COF_{Py\text{-}Bpy}$ predominantly localized at bipyridine units, indicating that bipyridine structures were more likely to act as acceptors. Moreover, the partial HOMO-LUMO overlap in $COF_{Py\text{-}PB}$ and $COF_{Py\text{-}Bpy}$, caused by strong polarization in the imine bonds, potentially hinders the donor-to-acceptor charge transfer. Compared to $COF_{Py\text{-}PB}$, the LUMO position of $HCOF_{Py\text{-}PB}$ was almost centered on the bipyridine molecules, and the LUMO and HOMO distributions of $HCOF_{Py\text{-}PB}$ were more uniform, indicating higher conductivity after protonation.[38] In contrast, after $COF_{Py\text{-}Bpy}$ was protonated to $HCOF_{Py\text{-}Bpy}$, the charge was redistributed. In particular, the LUMO energy level of $HCOF_{Py\text{-}Bpy}$ (−5.28 eV) was deeper than that of $COF_{Py\text{-}Bpy}$ (−2.01 eV), while the HOMO energy level of $HCOF_{Py\text{-}Bpy}$ (−6.42 eV) was deeper than that of $COF_{Py\text{-}Bpy}$ (−5.12 eV), showing a considerable increase in

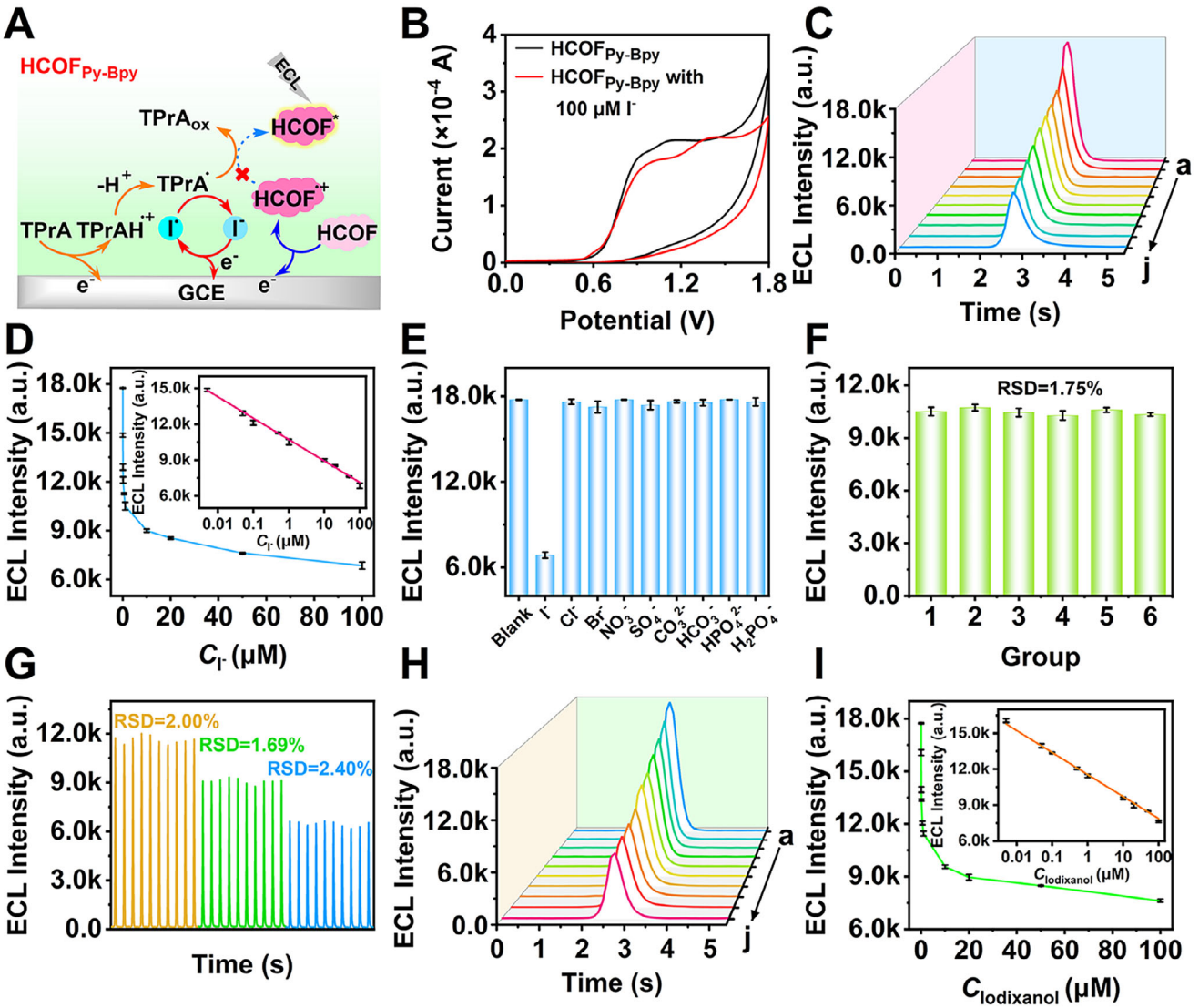

Figure 6. A) Mechanism of the ECL sensor for I^- detection. B) CV curves of $HCOF_{Py\text{-}Bpy}$/GCE in 20 mM TPrA in the absence and presence of I^-. C) ECL responses of $HCOF_{Py\text{-}Bpy}$/GCE to 0, 0.005, 0.05, 0.1, 0.5, 1, 10, 20, 50, and 100 μM I^- (a–j). (D) Plot of ECL intensity versus I^-concentration. Inset: Calibration curve. Error bars: mean ± SD, $n = 3$. E) ECL signals of 100 μM I^- in the presence of 1 mM interfering anions. F) Reproducibility of the ECL sensor in response to 1 μM I^-. Error bars: mean ± SD, $n = 6$. G) ECL-time profiles of the ECL sensor in response to 0.1 (orange), 10 (green), and 100 μM (blue) I^-. H) ECL responses of $HCOF_{Py\text{-}Bpy}$/GCE to 0, 0.005, 0.05, 0.1, 0.5, 1, 10, 20, 50, and 100 μM iodixanol (a–j). I) Plot of ECL intensity versus iodixanol concentration. Inset: Calibration curve. Error bars: mean ± SD, $n = 3$.

the degree of π-delocalization along the conjugated backbone, which was conducive to carrier migration.[39] The protonation of bipyridyl and imine nitrogen centers induced electron deficiency, transforming the bipyridine moiety into an effective electron-accepting unit. The band gap obtained from DFT calculation revealed that $HCOF_{Py\text{-}Bpy}$ possessed a narrower band gap (1.14 eV) than $COF_{Py\text{-}Bpy}$ (3.11 eV), while the band gap of $HCOF_{Py\text{-}PB}$ (1.43 eV) was narrower than that of $COF_{Py\text{-}PB}$ (3.16 eV), which was consistent with the position of the calculated energy level, indicating that the protonation was favorable for charge transfer. Introducing nitrogen atoms and implementing post-protonation amplified the D-A effect, leading to diminished exciton binding energy that promoted both exciton dissociation and charge separation.[40,41] Consequently, $HCOF_{Py\text{-}Bpy}$ exhibited enhanced D-A interaction relative to $COF_{Py\text{-}Bpy}$, effectively facilitating charge transfer. In addition, the electrostatic potential (ESP)[42] maps of COFs and HCOFs were generated based on the molecular fragments (Figure 5B). The negative potential mainly converged on the nitrogen atoms of bipyridine and imine in $COF_{Py\text{-}PB}$ and $COF_{Py\text{-}Bpy}$, while the positive potential was distributed in pyrenyl. However, the negative potential was opposite after protonation. $HCOF_{Py\text{-}Bpy}$ exhibited a dipole moment of 26.69 Debye (D), which was larger than that of $COF_{Py\text{-}Bpy}$ (3.22 D), and $HCOF_{Py\text{-}PB}$ (13.64 D) was also larger than that of $COF_{Py\text{-}PB}$ (1.86 D). Notably, $HCOF_{Py\text{-}Bpy}$ exhibited a greater dipole moment than $HCOF_{Py\text{-}PB}$, demonstrating that protonation enhanced molecular polarization. The increased polarization facilitated the formation of a robust internal electric field to boost the charge

separation effect.[32,43–45] Moreover, the surface charge density further revealed their charge separation capability.[46] The surface potentials (ΔE) of $COF_{Py\text{-}PB}$, $COF_{Py\text{-}Bpy}$, $HCOF_{Py\text{-}PB}$, and $HCOF_{Py\text{-}Bpy}$ obtained through Kelvin probe force microscope (KPFM) are 26.55, 34.79, 48.52, and 74.62 mV, respectively (Figure 5C; Figure S10, Supporting Information). The greater surface potential supported the presence of a stronger intramolecular charge separation driving force in $HCOF_{Py\text{-}Bpy}$, which significantly promoted the charge separation and transfer.

2.4. ECL Sensing Application for I–

I^- is widely used in pharmaceutical manufacturing, especially in producing iodinated contrast agents (ICMs). These agents are vital for enhancing medical imaging in radiological examinations.[47] While iodixanol is among the safer ICMs, excessive doses may cause adverse effects, including allergic reactions and hypertension.[48,49] Thus, developing sensitive and rapid detection methods is crucial. To verify the application of the enhanced ECL performance, a sensitive ECL sensor for I^- was constructed (**Figure 6A**). The CV curve of $HCOF_{Py\text{-}Bpy}$/GCE showed an extra oxidation peak at +0.60 V, which closely matched the oxidation potential of I^- at +0.56 V, indicative of I^- oxidation to iodine radical ($I^•$) (Figure 6B; Figure S11A, Supporting Information). The resulting $I^•$ could react with $TPrA^•$ to produce I^- for further quenching cycles. As a result, it suppressed the electron transfer between $TPrA^•$ and $HCOF_{Py\text{-}Bpy}{}^{•+}$, ultimately quenching the ECL signal. With the increasing I^-concentration, the ECL intensity of $HCOF_{Py\text{-}Bpy}$ decreased progressively and showed a linear negative correlation with the logarithm of the I^-concentration (Figure 6C,D). The linear regression equation was $I_{ECL} = 10\ 713.96 - 1787.92 \lg C$ with a correlation coefficient (R^2) of 0.9971. The limit of detection was determined to be 0.11 nM based on the control group plus 3 times the standard deviation. Compared with those previous reports, this ECL sensor possessed better sensitivity (Table S1, Supporting Information).

The selectivity of the ECL sensor was examined at 100 µM I^- with 1 mM interfering anions, which showed negligible change in the ECL intensity (Figure 6E), indicating excellent selectivity. The reproducibility of the sensors was further verified by six parallel measurements, and the ECL signals showed very little variation with an RSD of 1.75% (Figure 6F). The ECL signals with RSDs less than 2.40% ($n = 10$) also demonstrated the excellent stability of the sensors (Figure 6G). The presence of iodixanol in the co-reactant system generated a peak at +1.44 V, matching its characteristic oxidation potential (+1.47 V), which simultaneously suppressed TPrA oxidation (Figure S11B,C, Supporting Information), demonstrating that iodixanol incorporation reduced the generation of excited-state $HCOF_{Py\text{-}Bpy}{}^*$, thus reducing ECL emission. The ECL emission intensity of the $HCOF_{Py\text{-}Bpy}$/GCE exhibited an iodixanol concentration-dependent quenching in a range of 0.005–100 µM (Figure 6H). The linear regression equation was $I = 11\ 550.10 – 1839.58 \lg C$ ($R^2 = 0.9974$), and the limit of detection was determined to be 0.39 nM (Figure 6I). The recovery experiments were performed by spiking I^- in Black Tiger Spring. The recoveries were from 97.6% to 103.2%, with RSDs of 1.93%–3.69% (Table S2, Supporting Information), indicating the feasibility of the proposed ECL sensor for real sample analysis.

3. Conclusion

In summary, we have developed a dual enhancement strategy to significantly enhance the ECL performance of imine-linked COFs. By strategically incorporating bipyridine units and implementing a post-synthetic modification protocol, we achieve the simultaneous protonation of both bipyridine and imine nitrogen sites in the COF. The duplex-protonated $HCOF_{Py\text{-}Bpy}$ demonstrates a robust built-in electric field, a reduced bandgap, and enhanced hydrophilicity to significantly improve the ECL performance, which enhances the ECL intensity by 9.63 and 4.11 times compared to COFs without protonation and with protonated imine nitrogen, and achieves an ECL efficiency up to 20.85%. DFT calculations validate that the protonation enhances the electron-withdrawing effect and induces a large dipole moment to reinforce the D-A interaction. A simple ECL sensing method for I^- or/and iodixanol with excellent analytical performance has also been proposed with the $HCOF_{Py\text{-}Bpy}$ to demonstrate the practical application of the post-synthetic protonation of COFs in the ECL sensing field, indicating an efficient avenue for designing the advanced ECL-active COF emitters.

4. Experimental Section

Synthesis of $HCOF_{Py\text{-}PB}$ and $HCOF_{Py\text{-}Bpy}$: As-synthesized $COF_{Py\text{-}PB}$ or $COF_{Py\text{-}Bpy}$ (10 mg) were put into L-ascorbic acid (1 M). After stirring for 10 min, the precipitates were filtered and washed with deionized water, and finally dried overnight under vacuum at 60 °C to obtain the protonated $HCOF_{Py\text{-}PB}$ or $HCOF_{Py\text{-}Bpy}$.

ECL and Electrochemical Measurements: The ECL and electrochemical measurements were performed using a three-electrode system with a 4-mm diameter GCE as the working electrode, a Pt counter electrode, and a reference electrode (Ag/AgCl, saturated) in a quartz electrolytic cell. The ECL measurements were carried out by scanning the potential from 0 to +0.8 V in 0.1 M PBS (pH 7.4) containing 20 mM TPrA with a photomultiplier tube (PMT) voltage of 850 V and a scan rate of 0.3 V/s. The CV was measured at a scan rate of 0.1 V/s.

Supporting Information

Supporting Information is available from the Wiley Online Library or from the author.

Acknowledgements

X.C. and W.G. contributed equally to this work. This work was supported by the National Natural Science Foundation of China (Grant Nos. 21974080), National Science Foundation of Shandong Province (ZR2025MS264), and the State Key Laboratory of Analytical Chemistry for Life Science (SKLACLS2306). The authors extend their gratitude to Scientific Compass (https://www.shiyanjia.com) for providing invaluable assistance with the TEM analysis. Thanks to eceshi (https://www.eceshi.com) for the KPFM analysis.

Conflict of Interest

The authors declare no competing financial interest.

Data Availability Statement

The data that support the findings of this study are available from the corresponding author upon reasonable request.

Keywords

covalent organic frameworks, electrochemiluminescence, protonation, robust built-in electric field, sensor

Received: September 5, 2025
Revised: October 21, 2025
Published online:

[1] Q. Gu, J. Zha, C. Chen, X. Wang, W. Yao, J. Liu, F. Kang, J. Yang, Y. Y. Li, D. Lei, Z. Tang, Y. Han, C. Tan, Q. Zhang, *Adv. Mater.* **2024**, *36*, 2306414.
[2] Q. Gu, X. Lu, C. Chen, X. Wang, F. Kang, Y. Y. Li, Q. Xu, J. Lu, Y. Han, W. Qin, Q. Zhang, *Angew. Chem., Int. Ed.* **2024**, *63*, 202409708.
[3] J. Yang, F. Kang, X. Wang, Q. Zhang, *Mater. Horiz.* **2022**, *9*, 121.
[4] F. Kang, X. Wang, C. Chen, C.-S. Lee, Y. Han, Q. Zhang, *J. Am. Chem. Soc.* **2023**, *145*, 15465.
[5] Y. Yang, M. Faheem, L. Wang, Q. Meng, H. Sha, N. Yang, Y. Yuan, G. Zhu, *ACS Cent. Sci.* **2018**, *4*, 748.
[6] B.-B. Luan, X. Chu, Y. Wang, X. Qiao, Y. Jiang, F.-M. Zhang, *Adv. Mater.* **2024**, *36*, 2412653.
[7] G. Lin, H. Ding, D. Yuan, B. Wang, C. Wang, *J. Am. Chem. Soc.* **2016**, *138*, 3302.
[8] S. Song, D. Wang, K. Zhao, Y. Wu, P. Zhang, J. Liu, G. Yang, P. Gong, Z. Liu, *Chem. Eng. J.* **2022**, *442*, 135963.
[9] Y. Zhao, S. Das, T. Sekine, H. Mabuchi, T. Irie, J. Sakai, D. Wen, W. Zhu, T. Ben, Y. Negishi, *Angew. Chem., Int. Ed.* **2023**, *62*, 202300172.
[10] F. Hao, C. Yang, X. Lv, F. Chen, S. Wang, G. Zheng, Q. Han, *Angew. Chem., Int. Ed.* **2023**, *62*, 202315456.
[11] D. Chen, W. Chen, Y. Wu, L. Wang, X. Wu, H. Xu, L. Chen, *Angew. Chem., Int. Ed.* **2023**, *62*, 202217479.
[12] J. Yang, A. Acharjya, M.-Y. Ye, J. Rabeah, S. Li, Z. Kochovski, S. Youk, J. Roeser, J. Grüneberg, C. Penschke, M. Schwarze, T. Wang, Y. Lu, R. van de Krol, M. Oschatz, R. Schomäcker, P. Saalfrank, A. Thomas, *Angew. Chem., Int. Ed.* **2021**, *60*, 19797.
[13] P. Dong, X. Xu, T. Wu, R. Luo, W. Kong, Z. Xu, S. Yuan, J. Zhou, J. Lei, *Angew. Chem., Int. Ed.* **2024**, *63*, 202405313.
[14] Y. Wang, G. Zhao, H. Chi, S. Yang, Q. Niu, D. Wu, W. Cao, T. Li, H. Ma, Q. Wei, *J. Am. Chem. Soc.* **2021**, *143*, 504.
[15] A. Zanut, F. Palomba, M. Rossi Scota, S. Rebeccani, M. Marcaccio, D. Genovese, E. Rampazzo, G. Valenti, F. Paolucci, L. Prodi, *Angew. Chem., Int. Ed.* **2020**, *59*, 21858.
[16] J. Descamps, C. Colin, G. Tessier, S. Arbault, N. Sojic, *Angew. Chem., Int. Ed.* **2023**, *135*, e202218574.
[17] L. Hu, G. Xu, *Chem. Soc. Rev.* **2010**, *39*, 3275.
[18] R. Luo, H. Lv, Q. Liao, N. Wang, J. Yang, Y. Li, K. Xi, X. Wu, H. Ju, J. Lei, *Nat. Commun.* **2021**, *12*, 6808.
[19] D. Zhu, Y. Zhang, S. Bao, N. Wang, S. Yu, R. Luo, J. Ma, H. Ju, J. Lei, *J. Am. Chem. Soc.* **2021**, *143*, 3049.
[20] Y.-J. Li, W.-R. Cui, Q.-Q. Jiang, Q. Wu, R.-P. Liang, Q.-X. Luo, J.-D. Qiu, *Nat. Commun.* **2021**, *12*, 4735.
[21] X. Meng, L. Zheng, R. Luo, W. Kong, Z. Xu, P. Dong, J. Ma, J. Lei, *Angew. Chem., Int. Ed.* **2024**, *63*, 202402373.
[22] J.-L. Zhang, L.-Y. Yao, Y. Yang, W.-B. Liang, R. Yuan, D.-R. Xiao, *Anal. Chem.* **2022**, *94*, 3685.
[23] L. Dai, A. Dong, X. Meng, H. Liu, Y. Li, P. Li, B. Wang, *Angew. Chem., Int. Ed.* **2023**, *62*, 202300224.
[24] L. Li, L. Xu, Z. Hu, J. C. Yu, *Adv. Funct. Mater.* **2021**, *31*, 2106120.
[25] X. Wang, L. Chen, S. Y. Chong, M. A. Little, Y. Wu, W.-H. Zhu, R. Clowes, Y. Yan, M. A. Zwijnenburg, R. S. Sprick, A. I. Cooper, *Nat. Chem.* **2018**, *10*, 1180.
[26] J. Kou, G. Wang, H. Guo, L. Li, J. Fang, J. Ma, Z. Dong, *Appl. Catal. B: Environ. Energy* **2024**, *352*, 124020.
[27] X. Gao, J. Yuan, P. Wei, J. Dong, L. Chang, Z. Huang, H. Zheng, J. Liu, J. Jia, T. Luan, B. Zhou, H. Yu, C. Peng, *ACS Catal.* **2024**, *14*, 533.
[28] L. Ascherl, E. W. Evans, J. Gorman, S. Orsborne, D. Bessinger, T. Bein, R. H. Friend, F. Auras, *J. Am. Chem. Soc.* **2019**, *141*, 15693.
[29] W. Dong, Z. Qin, K. Wang, Y. Xiao, X. Liu, S. Ren, L. Li, *Angew. Chem., Int. Ed.* **2023**, *62*, 202216073.
[30] W. Cao, R. Yuan, H. Wang, *Anal. Chem.* **2023**, *95*, 7640.
[31] Y. Wang, Y.-Z. Cheng, K.-M. Wu, D.-H. Yang, X.-F. Liu, X. Ding, B.-H. Han, *Angew. Chem., Int. Ed.* **2023**, *62*, 202310794.
[32] H. Ben, G. Yan, H. Liu, C. Ling, Y. Fan, X. Zhang, *Adv. Funct. Mater.* **2022**, *32*, 2104519.
[33] L. Cui, Y. Yang, L. Song, X. Cao, W. Chu, C.-Y. Zhang, *Small* **2025**, *21*, 2408946.
[34] Y. Zhang, Y. Zhao, Z. Han, R. Zhang, P. Du, Y. Wu, X. Lu, *Angew. Chem., Int. Ed.* **2020**, *59*, 23261.
[35] Y. Cao, R. Yuan, Y. Chai, L. Mao, X. Yang, S. Yuan, Y. Yuan, Y. Liao, *Electroanalysis* **2011**, *23*, 1418.
[36] L. Yang, X. Sun, D. Wei, H. Ju, Y. Du, H. Ma, Q. Wei, *Anal. Chem.* **2021**, *93*, 1553.
[37] T. Lu, F. Chen, *J. Comput. Chem.* **2012**, *33*, 580.
[38] Y. Wang, Z. Qiao, H. Li, R. Zhang, Z. Xiang, D. Cao, S. Wang, *Angew. Chem., Int. Ed.* **2024**, *63*, 202404726.
[39] Q. Che, C. Li, Z. Chen, S. Yang, W. Zhang, G. Yu, *Angew. Chem., Int. Ed.* **2024**, *63*, 202409926.
[40] F. Liu, Y. He, X. Liu, Z. Wang, H.-L. Liu, X. Zhu, C.-C. Hou, Y. Weng, Q. Zhang, Y. Chen, *ACS Catal.* **2022**, *12*, 9494.
[41] L. Hao, R. Shen, C. Huang, Z. Liang, N. Li, P. Zhang, X. Li, C. Qin, X. Li, *Appl. Catal. B: Environ. Energy* **2023**, *330*, 122581.
[42] J. Zhang, T. Lu, *Phys. Chem. Chem. Phys.* **2021**, *23*, 20323.
[43] Z. Chen, J. Wang, M. Hao, Y. Xie, X. Liu, H. Yang, G. I. N. Waterhouse, X. Wang, S. Ma, *Nat. Commun.* **2023**, *14*, 1106.
[44] C. Wu, Z. Teng, C. Yang, F. Chen, H. B. Yang, L. Wang, H. Xu, B. Liu, G. Zheng, Q. Han, *Adv. Mater.* **2022**, *34*, 2110266.
[45] K. Wu, X.-Y. Liu, M. Xie, P.-W. Cheng, J. Zheng, W. Lu, D. Li, *Appl. Catal. B: Environ. Energy* **2023**, *334*, 122847.
[46] J. Jing, J. Yang, Z. Zhang, Y. Zhu, *Adv. Energy Mater.* **2021**, *11*, 2101392.
[47] G. Vassaux, C. Zwarthoed, L. Signetti, J. Guglielmi, C. Compin, J.-M. Guigonis, T. Juhel, O. Humbert, D. Benisvy, T. Pourcher, B. Cambien, *J. Nucl. Med.* **2018**, *59*, 121.
[48] T.-M. Chiu, S.-Y. Chu, *Biomedicines* **2022**, *10*, 1036.
[49] W. Zhang, W. Yuan, H.-L. Yuan, X.-L. Yang, H. Xie, *Clin. Toxicol.* **2017**, *55*, 939.